Fibers and Polymers 2004, Vol.5, No.2, 160-169

Processing of Microcellular Nanocomposite Foams by Using a Supercritical Fluid

Dongho Wee, Dong Gi Seong, and Jae Ryoun Youn*

School of Materials Science and Engineering, Seoul National University, Seoul 151-742, Korea
(Received December 1, 2003; Revised May 7, 2004; Accepted May 14, 2004)

Abstract: Polystyrene/layered silicate nanocomposites were prepared by melt intercalation. To examine the distribution of the clay in polymer matrix, small angle X-ray scattering (SAXS) and transmission electron microscopy (TEM) were used. Intercalated nanocomposites were obtained and their rheological properties were investigated. Microcellular nanocomposite foams were produced by using a supercritical fluid. As clay contents increased, the cell size decreased and the cell density increased. It was found that layered silicates could operate as heterogeneous nucleation sites. As the saturation pressure increased and the saturation temperature decreased, the cell size decreased and the cell density increased. Microcellular foams have different morphology depending upon the dispersion state of nanoclays.

Keywords: Nanocomposite, Melt intercalation, Microcellular foam, Supercritical fluid, Heterogeneous nucleation

Introduction

Nanocomposites are composite materials consisting of building blocks in the nanometer or tens of nanometer size scales [1]. Many studies on polymer/layered silicate nanocomposites have been reported since the development of the Nylon-6/montmorillonite nanocomposites by Toyota Motors group [2]. Conventional polymer composites usually require a large amount of fillers (more than 10 wt%) to obtain desired mechanical properties. The high filler content causes many problems, such as weight increase, high torque needed for mixing, and poor dispersion in matrix. On the other hand, polymer/layered silicate nanocomposites exhibit increase in mechanical properties [3,4], barrier properties [5,6], and heat resistance [7]. The increase in the properties is caused by the structure of polymer/layered silicate nanocomposites. Polymer/layered silicate nanocomposites are commonly fabricated through in-situ polymerization or melt intercalation. During in-situ polymerization, interlayer distances are expanded by polymerization of monomers between the interlayers of the layered silicate. As a result, silicate layers are homogeneously dispersed at the end of the polymerization. During melt intercalation, the layered silicate is mixed with polymer matrix in the molten state. If the layer surfaces are compatible with the polymer matrix, macromolecules will penetrate into the interlayer space and the layered silicate will be delaminated. For the melt intercalation, twin-screw extruder is usually used as a mixing equipment to aid the delamination of silicate layers with mechanical shearing. The melt intercalation is more preferable method to produce nanocomposites for commercial use because no solvent is required and the fabrication is simple. Besides these methods, the solvent method is also employed. The layered silicate is firstly exfoliated into single layers by using a solvent in which the polymer is solubles, and nanocomposites are obtained by removing the solvent.

Microcellular foam is a closed-cell foam which contains gas bubbles of diameters on the order of 10 μm with cell density in the range of 10^9 to 10^{15} cells/cm^3 [8-16]. It is known that the microcellular foam shows higher impact strength [17], higher toughness [18], increased fatigue life [19], and enhanced thermal stability [20] compared with other plastic foams. These improvements are due to the presence of cells that are much smaller than those of conventional foams. The presence of microcells can reduce the specific density of the polymer by about 75 % [21]. Microcellular foam was developed by Suh and his co-workers in the early 1980's [22]. Microcellular foaming process consists of two stages. In the first stage, the polymer sample is placed in a pressure vessel and saturated with a non-reactive gas (such as N_2, CO_2) at room temperature and moderate pressure (about 2~6 MPa). In the second stage, the saturated sample is heated in an oil bath above the glass transition temperature (T_g). The sudden increase in temperature causes cell nucleation and growth and results in foam structure with cell sizes on the order of 10 micrometers.

A different foaming process was developed by Goel and Beckman [23,24]. A polymer sample is saturated with supercritical CO_2 and the microcellular foam is obtained by a rapid depressurization. Supercritical fluids (SCFs) are obtained above their critical pressure and temperature. Supercritical fluids act as good solvents due to the liquid property and have high diffusivity due to the gas property. These properties ensure rapid swelling of polymers [23]. Supercritical fluids have advantages when used as the physical blowing agent because they will depress the glass transition temperature of polymers and avoid the vapor/liquid boundary, which can damage the cellular structure. Critical temperature of carbon dioxide is 304.15 K and its critical pressure is 7.38 MPa.

In this study, polystyrene/organophilic montmorillonite (OMMT) nanocomposites were prepared by the melt

*Corresponding author: jaeryoun@snu.ac.kr

intercalation. Microcellular foams were produced by the method which had been proposed by Goel and Beckman. The main objective of this study is to investigate the influence of nanoclay to the structure of microcellular foam and develop the process for producing the nanocomposite foam with optimum structure by using a supercritical fluid.

Experimental

Preparation of Nanocomposites

A commercially available GPPS (General Purpose Polystyrene, HF-2680 which was provided by Cheil Industries Inc.) was used for preparation of nanocomposites. Two different OMMTs were used, Cloisite® 15A and Cloisite® 30B, which were supplied by Southern Clay Products, Inc. These materials were dried at 60 °C over 24 hr prior to use. Polystyrene/OMMT nanocomposites were prepared by using a intermeshing twin-screw extruder (PLASTI-CORDER® PLE-651, BRABENDER®) operated in the counter-rotating mode at operating temperature of 200 °C. PS/15A nanocomposites with three different OMMT contents of 3, 5, and 7 wt%, which were named as PS15A3, PS15A5, PS15A7, were extruded at the screw speed of 70 rpm. PS/30B nanocomposites with OMMT content of 5 wt%, named as PS30B5, was extruded at a screw speed of 20 rpm intentionally to give a relatively poor dispersion. Specimens for the foaming experiment were fabricated in the shape of disc (1.5 mm in thickness and 20 mm in diameter) by using a hot press (WABASH®) at 220 °C for 5 min.

Microcellular Foaming

Figure 1 shows the experimental set-up for production of

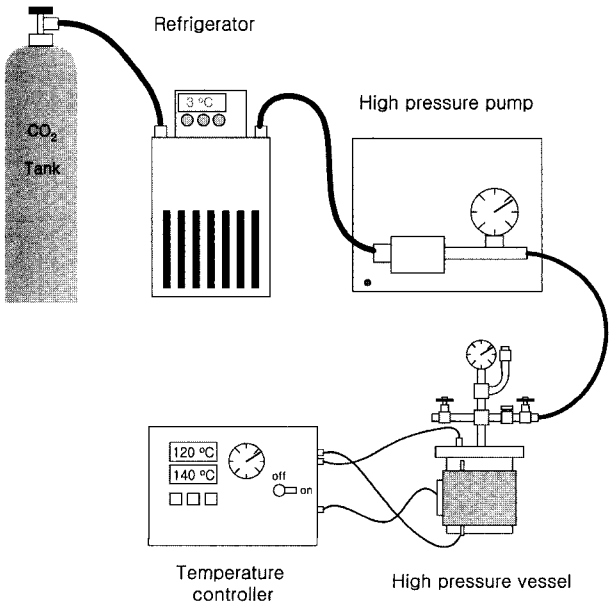

Figure 1. Experimental set-up for fabrication of microcellular foam.

Table 1. Foaming conditions used in this study

Clay used	Clay content (wt%)	Saturation pressure, P_s (MPa)	Saturation temperature, T_s (°C)
Cloisite® 15A	0	12	100
	3		
	5		
	7		
	5	8	100
		10	
		12	
		14	
		16	
		12	80
			100
			120
Cloisite® 30B	5	12	100

the microcellular foam. Microcellular foams were prepared in the high pressure vessel containing a Teflon® support which was used to avoid sticking of the specimen to the vessel wall. The high pressure vessel was preheated to the desired temperature and the specimen was placed in the vessel. The vessel was filled with supercritical CO_2 that had been passed through the refrigerator to maintain liquid state of CO_2 and pressurized at the desired pressure using the high pressure pump (THAR®, P-50). Both the foaming temperature and pressure were over critical point of CO_2. The vessel was rapidly depressurized by opening the venting valve after a sufficient saturation period (24 hr). After depressurization, the foamed sample was removed from the vessel and cooled at room temperature. Table 1 shows foaming conditions used in this study.

Characterization

The intercalated structure of nanocomposites was investigated by employing small angle X-ray scattering with the Rigaku Max-3 Cg X-ray diffractometer (40 kV, 35 mA) with Cu Kα radiation (λ = 0.154184 nm). The scan angle (2θ) was from 1 ° to 8 °, and the scan rate was 8 °/hr. The interlayer distance was obtained from the Bragg's equation. TEM, Jeol JEM-2000EXII 200 kV, was used for the exact characterization of the nanocomposite morphology. TEM specimens were microtomed to an ultra thin section with a thickness of about 80 nm and coated with carbon for 7 min to prevent specimens from degradation caused by the irradiation of electrons.

SEM, Jeol JSM-6330F 5 kV, was used to characterize the morphology of microcellular foams. SEM specimens were obtained by fracturing the foam in liquid N_2. They were coated with Pt for 5 min prior to measurement. In order to determine the average cell diameter from SEM images of

cross-sections, an image processing software, Image-Pro® plus (Media Cybernetics®), was used. From the knowledge of stereology, the average cell diameter is obtained by using the following equation [25],

$$D = \frac{4}{\pi} d_{cell} \quad (1)$$

where D is average diameter of the spherical cell and d_{cell} is average diameter of craters on the cross-section. Cell density (number of cells per cm^3), N_f can be expressed as the following,

$$N_f = \left(\frac{nM^2}{A}\right)^{3/2} \quad (2)$$

where A is the area (cm^2) of the SEM image, M is the magnification factor and n is the number of cells in the SEM image [23]. The bulk foam density was measured by dividing the mass by the volume. Volume of the foamed specimen was measured by submerging it in the water.

Results and Discussion

Structure of Nanocomposites

Figures 2 and 3 show SAXS patterns of PS/15A and PS/30B nanocomposites respectively. In Figure 2(d), the clay peak was observed at 2.79 ° corresponding to an interlayer distance of d = 3.17 nm. However, peaks of nanocomposites were shifted to the lower angle compared with the peak of 15A (Figure 2(a)~(c)). Their peaks were located at 2.43 °~2.48 ° corresponding to the interlayer spacing of d = 3.56~3.64 nm. The increase of interlayer distance is due to the swelling of interlayers by penetration of polymer chains, which indicates that PS/15A nanocomposites had intercalated structure. On the other hand, the peak of PS30B5 in Figure 3(b) was shifted to the higher angle compared with the peak of 30B (Figure 3(a)), i.e., the interlayer distance decreased from the original interlayer distance of 30B. The decrease in

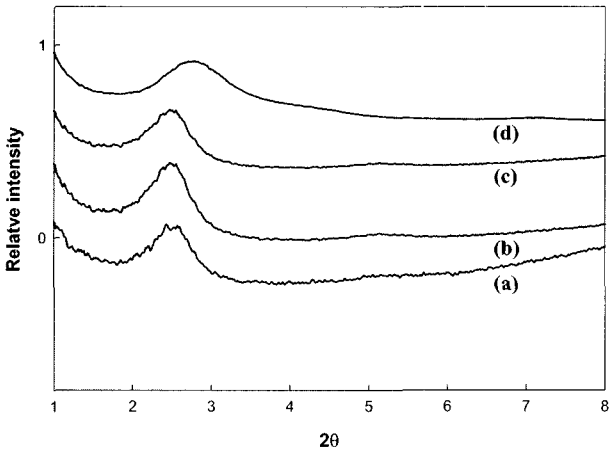

Figure 2. SAXS patterns of (a) PS15A3, (b) PS15A5, (c) PS15A7, and (d) 15A.

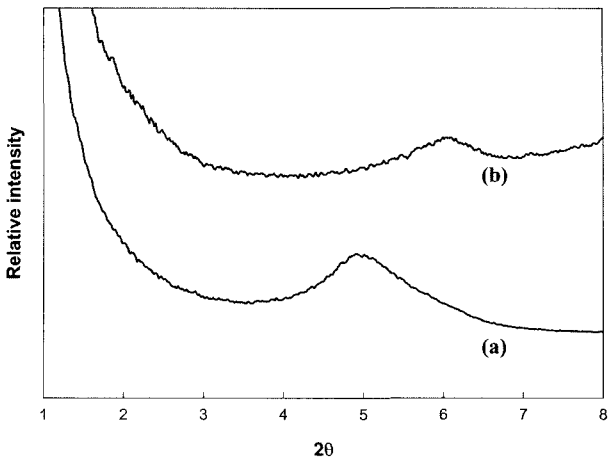

Figure 3. SAXS patterns of (a) 30B and (b) PS30B5.

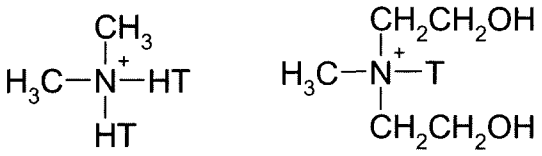

(a) (b)

Figure 4. Organic cations in (a) Cloisite® 15A and (b) Cloisite® 30B (HT is hydrogenated tallow: ~65 % C18, ~30 % C16, ~5 % C14).

the interlayer distance can be explained as follows. As shown Figure 4, the organic material in 30B is hydrophilic due to existence of hydroxide groups. Therefore, it is not probable for polystyrene chains with strong hydrophobic phenyl groups to penetrate into 30B. In addition, thermal degradation of organic materials on clay layer surfaces can occur at high temperature. If the polymer is compatible with the clay, the interlayer distance will not decrease because polymer chains which penetrate into the gallery prevent the interlayer from contraction. However, the interlayer contraction occurs prior to the penetration of polymer chains due to poor compatibility in the case of PS/30B system. Results from SAXS patterns are summarized in Table 2. The intercalated structure of PS/15A nanocomposites can be confirmed by

Table 2. Interlayer distances and peak diffraction angles obtained from the SAXS patterns

Sample	Peak position (2θ)	Interlayer distance (nm)
15A	2.79	3.17
PS15A3	2.43	3.64
PS15A5	2.47	3.58
PS15A7	2.48	3.56
30B	5.11	1.73
PS30B5	5.99	1.48

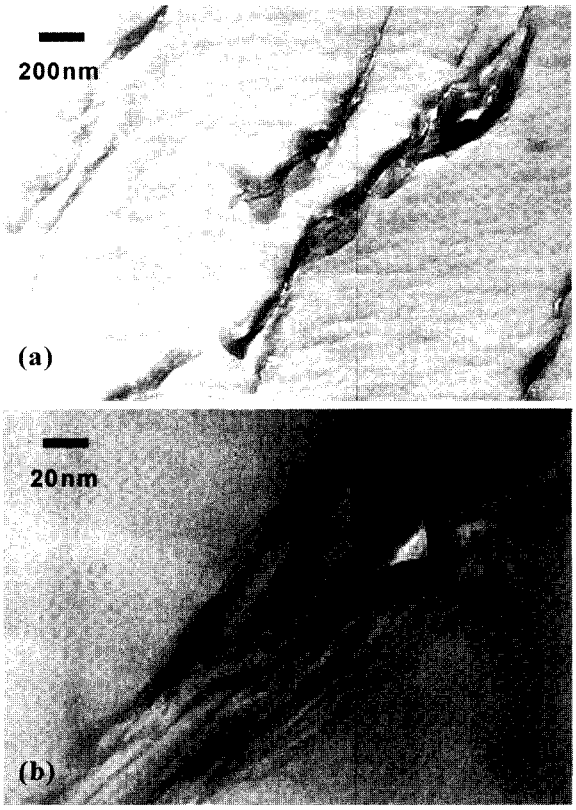

Figure 5. TEM images of the PS15A3: (a) ×20,000 and (b) ×200,000.

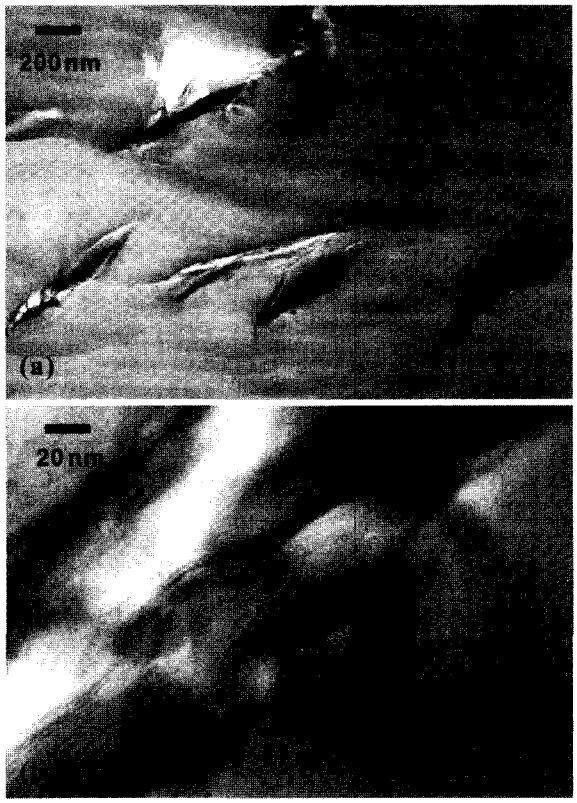

Figure 6. TEM images of the PS15A5: (a) ×20,000 and (b) ×200,000.

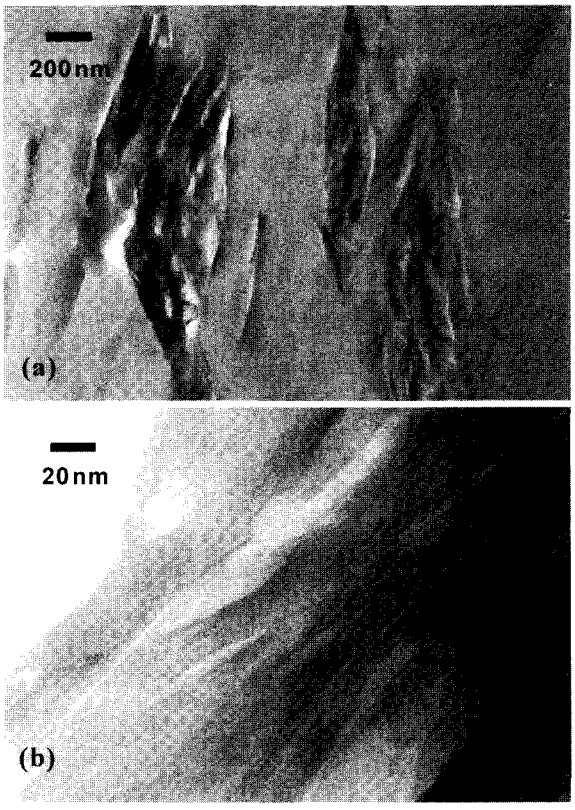

Figure 7. TEM images of the PS15A7: (a) ×20,000 and (b) ×200,000.

the TEM images shown in Figures 5 to 7. The dark lines in the figure correspond to the layered silicate. In the low magnification image, the phase separation of 15A is observed. But, one can observe that the stack of silicate layers is expanded in the high magnification image. Although the interlayer distance in PS/15A nanocomposites is increased, the exfoliated structure is not achieved. The failure in achieving exfoliation in PS/15A nanocomposites is explained by poor compatibility between PS and 15A.

Rheological Properties

Small amplitude oscillatory shear experiments were conducted in the linear regime at 200 °C. Figures 8 and 9 show storage modulus, G', and loss modulus, G", of PS/15A and PS/30B nanocomposites. One can see that G' and G" for nanocomposites increase monotonically with increasing clay contents and are higher compared with pure PS. However, G' and G" become similar at high frequencies. It means that the viscoelastic response is not affected by the existence of the layered silicate at high frequencies. In other words, the chain relaxation modes are not altered by the presence of the layered silicate [26]. As clay contents are increased, effects of the frequency on G' become smaller at low frequencies. This behavior is similar to the typical behavior of heterogeneous systems to which fillers are added. Figure 10 shows the complex viscosity, η^*, of pure PS and PS/15A nanocomposites. The

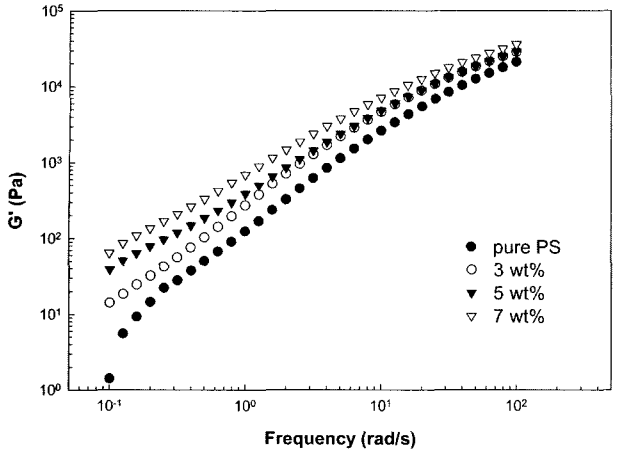

Figure 8. Storage modulus of PS/15A nanocomposites.

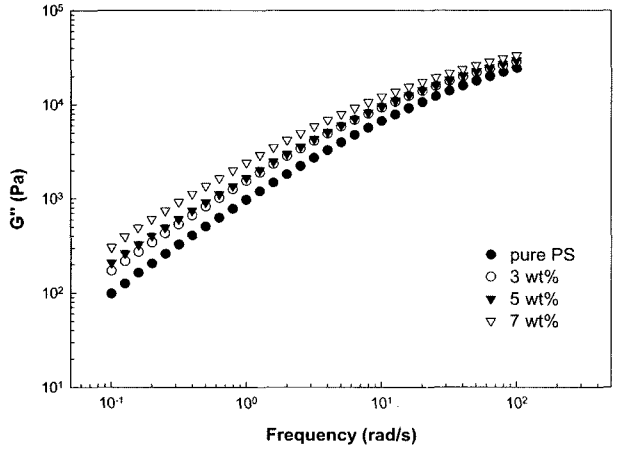

Figure 9. Loss modulus of PS/15A nanocomposites.

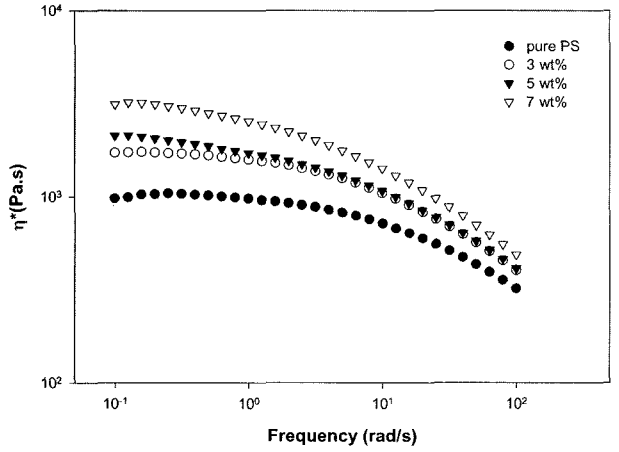

Figure 10. Complex viscosity of PS/15A nanocomposites.

complex viscosity is enhanced considerably at low shear rates and increases with increasing clay loading. While the complex viscosity of pure PS shows Newtonian behavior at low shear rates, nanocomposites show shear-thinning behavior. At high shear rates where pure PS shows shear-thinning behavior, nanocomposites also show the same behavior. The rheological behavior is caused by intimate contact between the polymer and silicate layers, which leads to changes in the relaxation dynamics of polymer chains.

Structure of Microcellular Foams

Effect of Clay Content

Scanning electron micrographs of the microcellular foam with respect to clay contents are shown in Figure 11. Closed and homogeneous cells are obtained for the specimens produced with the saturation pressure of 12 MPa and the temperature of 100 °C. Nanoclay of 3 wt% greatly reduces the cell diameter and increases the cell density as shown in Figures 12 and 13. Addition of 5 wt% clay further reduces the cell diameter and increases the cell density. These results can be explained by the classical nucleation theory which was suggested by Colton and Suh [27].

$$r^* = \frac{2\gamma_{bp}}{\Delta P} \tag{3}$$

Equation (3) predicts the critical radius of the bubble for homogeneous nucleation. Where γ_{bp} is the interfacial tension of the polymer-bubble interface, and ΔP is the pressure of the gas in the bubble. When the nucleus reaches the critical radius, the Gibbs free energy for homogeneous nucleation is maximum and given by the following equation.

$$\Delta G^*_{hom} = \frac{16\pi}{3\Delta P^2}\gamma_{bp}^3 \tag{4}$$

The homogeneous nucleation rate, N_o, is given by

$$N_o = C_o f_o \exp\left(\frac{-\Delta G^*_{hom}}{kT}\right) \tag{5}$$

where C_o is the concentration of gas molecules in the polymer, f_o is a frequency factor of gas molecules joining the nucleus, and k is the Boltzman's constant. The Gibbs free energy at critical radius can be regarded as the energy barrier for the creation of nucleus. Therefore, the smaller Gibbs free energy at critical radiusis, the easier generation of the nucleusis. The nucleation rate increases with the decreasing critical free energy as shown in equation (5). For the heterogeneous nucleation, the critical radius is the same as that of the homogeneous nucleation. The critical Gibbs free energy for heterogeneous nucleation is given as follows,

$$\Delta G^*_{het} = \frac{16\pi\gamma_{bp}^3}{3\Delta P^2}S(\theta) = \Delta G^*_{hom}S(\theta) \tag{6}$$

where θ is the wetting angle, and $S(\theta)$ is a function depending only on the wetting angle. The nucleation rate for the heterogeneous nucleation is derived as follows,

$$N_1 = C_1 f_1 \exp\left(\frac{\Delta G^*_{het}}{kT}\right) \tag{7}$$

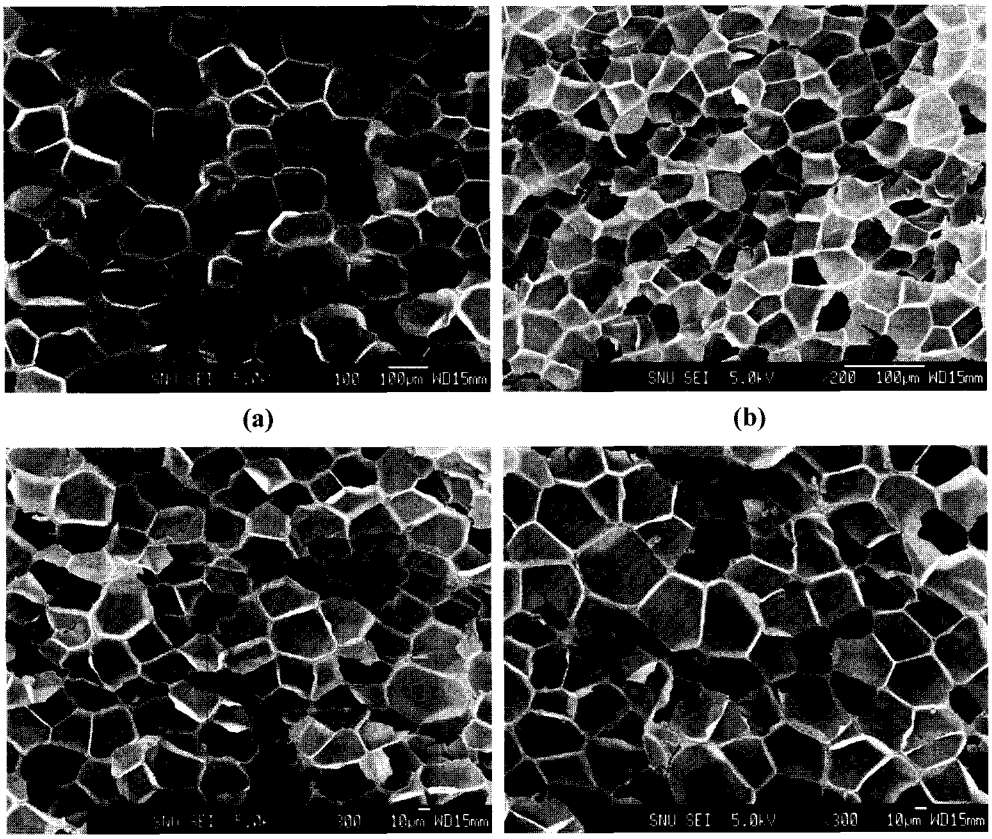

Figure 11. SEM images of the PS/15A nanocomposite foams for different clay contents. (P_s: 12 MPa, T_s: 100 °C): (a) Pure PS, (b) 3 wt%, (c) 5 wt%, and (d) 7 wt%.

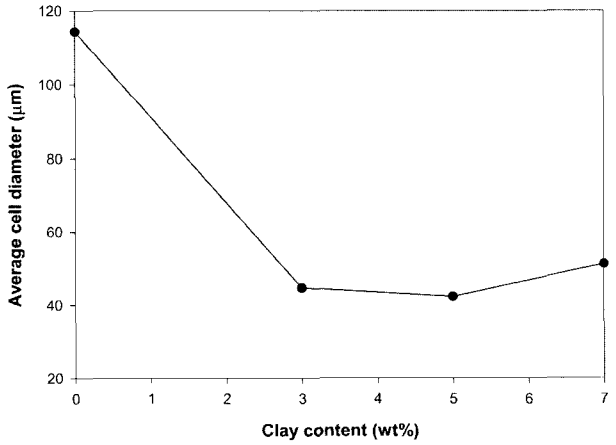

Figure 12. Effect of clay content on the average cell diameter of PS/15A nanocomposite foams (P_s: 12 MPa, T_s: 100 °C).

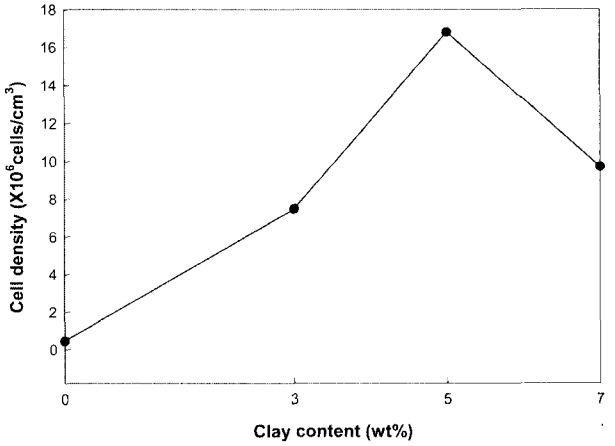

Figure 13. Effect of clay content on the cell density of PS/15A nanocomposite foams (P_s: 12 MPa, T_s: 100 °C).

where C_1 is the concentration of heterogeneous nucleation sites and f_1 is a frequency factor of gas molecules joining the nucleus. In equation (6), $S(\theta)$ is about 10^{-3} considering the contact angle. Therefore, the energy barrier for the heterogeneous nucleation becomes smaller than that of the homogeneous nucleation. Consequently the rate of heterogeneous nucleation will be higher than that of homogeneous nucleation. The layered silicates will act as nucleation sites and increase the

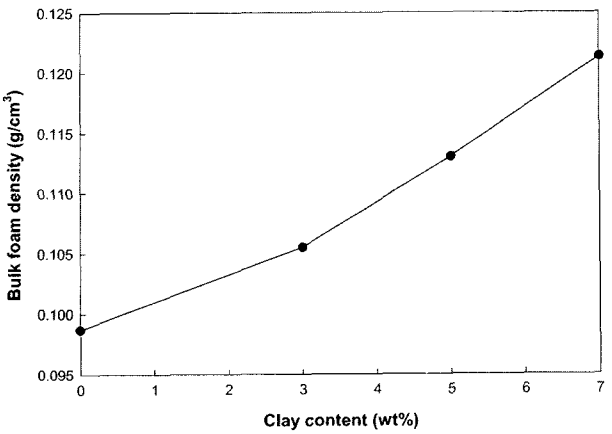

Figure 14. Effect of clay content on the bulk foam density of PS/15A nanocomposite foams (P_s: 12 MPa, T_s: 100 °C).

cell density. It is believed that the reduction of the energy barrier in the case of layered silicates is more effective than that in the case of conventional fillers because the nanoclay has larger surface area.

The cell diameter is affected by the cell growth dynamics. Once the cells have been nucleated, they continue to grow as the excess gas diffuses into the cells. As shown previously, the viscosity of the polymer increases when nanoclay is added. The increase of the viscosity hinders the cell growth, resulting in a smaller cell size. However, when 7 wt% of clay is added, the cell diameter increases. When a larger amount of nanoclay is added, the nucleation site is increased and the probability for cells to coalesce into a larger bubble is also increased. As a result, the cell diameter is increased and the cell density is reduced. In Figure 14, the bulk foam density is plotted with respect to the clay content. The bulk foam density also increases as more clay is added. The bulk foam density produced with 7 wt% of clay is higher than 5 wt% of clay although the cell diameter of the foam loaded with 7 wt% clay is larger than the foam loaded with 5 wt% clay. It is believed that the final bulk foam density is determined by the competition between the cell nucleation and the cell growth. The bulk foam density is also increased due to increase of mass by the addition of clays.

Effect of Saturation Pressure

The effect of saturation pressure on the foam structure has been studied for specimen prepared at a constant temperature of 100 °C with 5 wt% clay. Scanning electron micrographs of the microcellular foams are shown in Figure 15. The cell diameter and the cell density obtained from these pictures are shown in Figures 16 and 17. As the saturation pressure increases, the cell diameter decreases and the cell density increases. As shown in Figure 16, the cell diameter is reduced significantly with respect to the pressure change from 8 MPa to 10 Mpa. The cell density is increased sharply as the pressure is changed from 14 MPa to 16 MPa in Figure 17. In equation (4) and (6), the energy barrier for nucleation is inversely proportional to the square of the saturation pressure. Therefore,

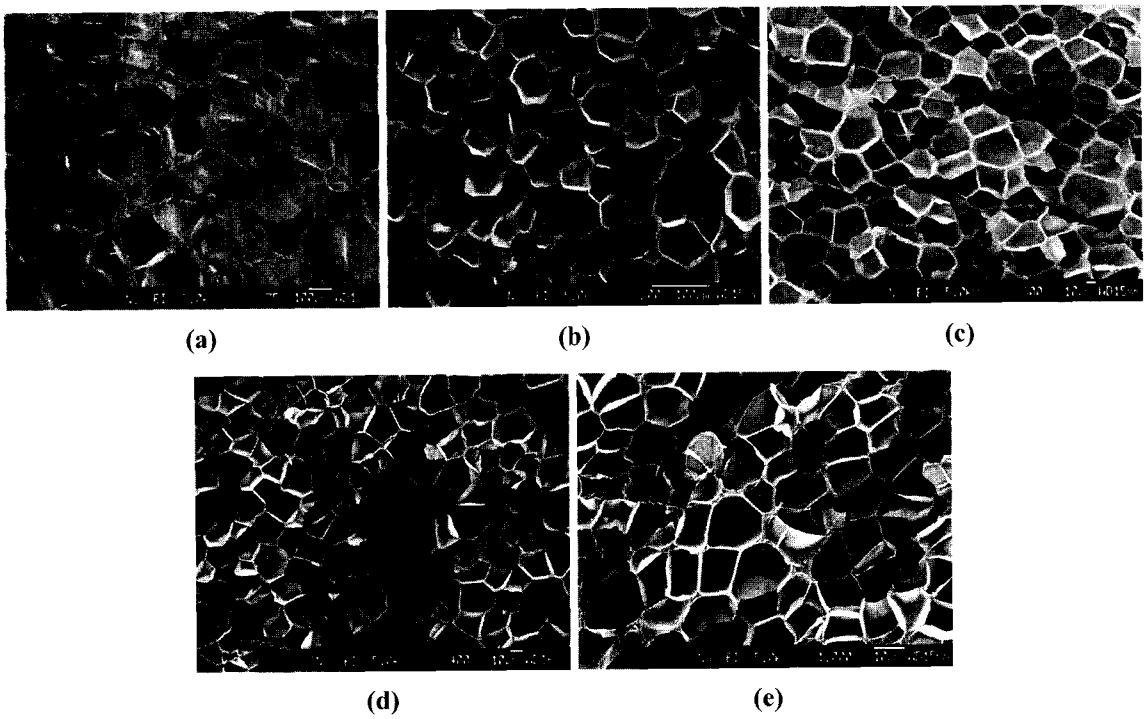

Figure 15. SEM images of the PS/15A nanocomposite foams produced at different saturation pressures (Clay content: 5 wt%, T_s: 100 °C): (a) 8, (b) 10, (c) 12, (d) 14, and (e) 16 MPa.

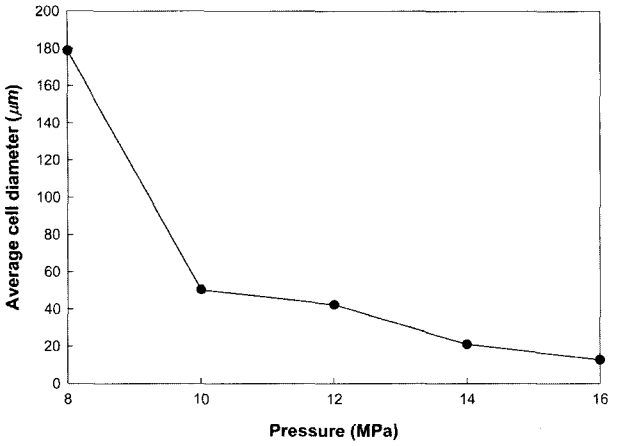

Figure 16. Effect of the saturation pressure on the average cell diameter of PS/15A nanocomposite foams (Clay content: 5 wt%, T_s: 100 °C).

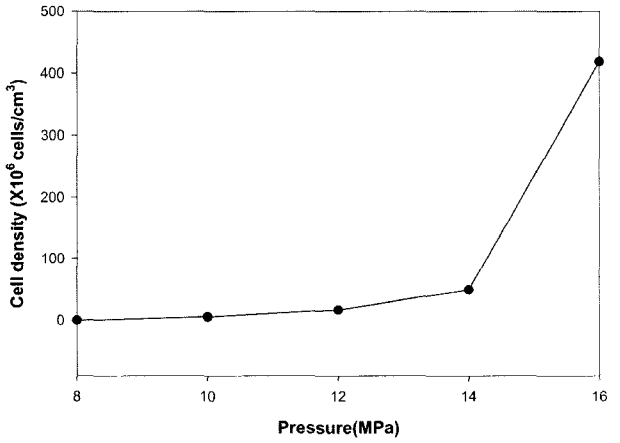

Figure 17. Effect of the saturation pressure on the cell density of PS/15A nanocomposite foams (Clay content: 5 wt%, T_s: 100 °C).

the energy barrier is reduced as the saturation pressure increases. The reduction of the energy barrier accelerates the nucleation rate as indicated in equation (5) or equation (7). The nucleation rate is also affected by the concentration of CO_2 in the polymer as known in equation (5). Solubility of CO_2 in PS increases with respect to the increase of saturation pressure [28]. In equation (5), the homogeneous nucleation rate increases in proportion to the concentration of gas molecules, C_o. Therefore, the cell density will increase as the saturation pressure increases.

Variation of the cell diameter with respect to the saturation pressure is explained by the cell nucleation rate and the cell growth rate. The amount of CO_2 gas allocated per each bubble is determined by the initial number of bubbles nucleated and the final size of the bubble is controlled by the cell growth mechanism. The cell growth is governed by diffusivity of CO_2 in the resin, the amount of CO_2 allocated per each bubble, viscosity of the resin, interfacial tension between the gas and

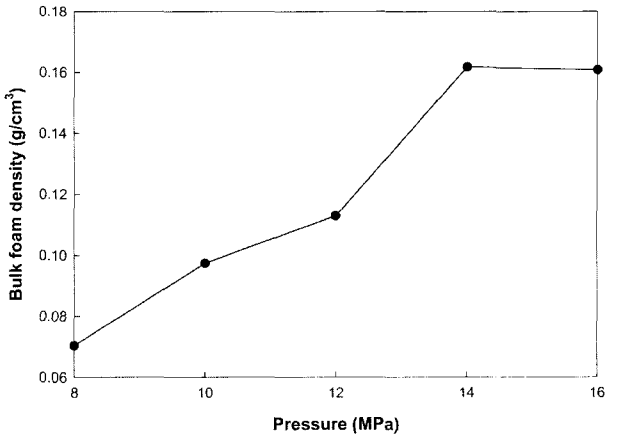

Figure 18. Effect of the saturation pressure on the bulk foam density of PS/15A nanocomposite foams (Clay content: 5 wt%, T_s: 100 °C).

the resin, gas concentration gradient outside the bubble, cooling rate of the resin, and rate of bubble coalescence. Figure 18 shows the bulk foam density with respect to the saturation pressure. It increases with increasing saturation pressure, and levels off at 16 MPa.

Effect of Saturation Temperature

The microcellular foams were obtained for different saturation temperature at 12 MPa with 5 wt% clay. The increase in saturation temperature led to increase in the cell diameter and decrease in the cell density. Since solubility of gas in the polymer matrix increases with decreasing temperature, the cell density increases as the saturation temperature decreases due to the increase in nucleation rate. As a result, the cell density increases as the saturation temperature decrease.

Effects of the saturation temperature on cell diameter can be explained by two respects, the cell growth time and the viscosity of the polymer matrix. The cell growth is finished when polymer is vitrified at a glass transition temperature, T_g (approximately 100 °C in PS). T_g is depressed when a supercritical fluid dissolved in the polymer matrix and it changes with the saturation pressure [29]. If the saturation temperature, T_s, is lower than T_g, $T_g - T_s$ becomes larger as T_s decreases. Therefore, higher pressure is required to depress T_g to temperature below T_s. In other words, vitrification will occur faster when higher saturation pressure is used [24]. When low saturation temperature is selected with high saturation pressure and the venting valve is opened after saturation, the time required for the pressure in the vessel to become equal to the pressure at which vitrification occurs, is shorter. When the saturation temperature is higher than T_g, the cell will grow for longer period of time. As a result, the cell diameter increases. The cell growth is influenced by the viscosity of the polymeric resin. The viscosity decreases as the saturation temperature increases and the decrease in the

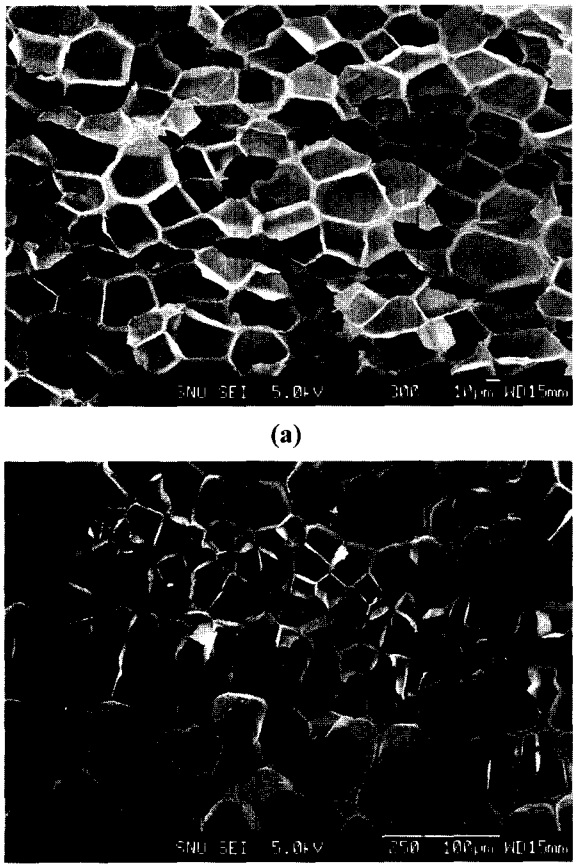

Figure 19. SEM images of the microcellular foams for different clay types (P_s: 12 MPa, T_s: 100 °C): (a) 15A and (b) 30B.

viscosity of polymeric resin enables the cells to grow easily.

Effect of Clay Type

Figure 19 shows SEM pictures of the microcellular foams for different clay types at the saturation pressure of 12 MPa and the saturation temperature of 100 °C with the same clay content, 5 wt%. It is observed that there is a big difference in morphologies between the PS15A5 and the PS30B5. PS15A5 has cells with uniform size and shape while PS30B5 shows a large deviation in the cell size and shape. The difference in the average cell diameter between PS15A5 and PS30B5 is small, but PS15A5 has higher cell density(16.779×10^6 cells/cm^3) compared with PS30B5 (9.6192×10^6 cells/cm^3). The higher cell density leads to decrease of the bulk foam density. These results are due to better clay dispersion in PS15A5 than in PS30B5. Due to poor compatibility between 30B and PS, layered silicates can remain as agglomerates in PS and provide agglomerated heterogeneous nucleation sites. Therefore, cells with non-uniform cell sizes and shapes are obtained. It is expected that foam with uniform cell size and shape can be generated if exfoliated nanocomposites are obtained. Better dispersion has to be obtained for production of microcellular foam filled with clay or other particulate additives.

Conclusions

Intercalated polystyrene/layered silicate nanocomposites were prepared by the melt intercalation. The microstructure was confirmed by SAXS and TEM. Due to intercalated structure between the polymer and layered silicates, modulus and viscosity were enhanced with increasing clay content. Microcellular nanocomposite foams were obtained by using supercritical CO_2 as the blowing agent. Addition of layered silicates dramatically reduced the cell size and increased the cell density because the layered silicates acted as heterogeneous nucleation sites. As the saturation pressure increased and the saturation temperature decreased, the cell size decreased and the cell density increased. The clay content, saturation pressure, and saturation temperature affected the cell morphology and the rheological properties of the nanocomposite foam. The cell morphology and the cell density were influenced significantly by the degree of clay dispersion.

Acknowledgement

This study was supported by the Korea Science and Engineering Foundation through the Applied Rheology Center (ARC), an officially KOSEF-created engineering research center at Korea University, Seoul, South Korea.

References

1. A. Lee and J. D. Lichtenhan, *J. Appl. Polym. Sci.*, **73**, 1993 (1999).
2. Y. Kojima, A. Usuki, M. Kawasumi, A. Okada, T. Kurauchi, and O. Kamigaito, *J. Polym. Sci., Part A, Polym. Chem.*, **31**, 1755 (1993).
3. A. Okada and A. Usuki, *Mater. Sci. Eng. C*, **3**, 109 (1995).
4. Z. Wang and T. J. Pinnavaia, *Chem. Mater*, **10**, 1820 (1998).
5. Y. Kojima, A. Usuki, M. Katasumi, A. Okada, T. Kurauchi, and O. Kamigaito, *J. Appl. Polym. Sci.*, **49**, 1259 (1993).
6. K. Yano, A. Usuki, and A. Okada, *J. Polym. Sci., Part A, Polym. Chem.*, **35**, 2289 (1997).
7. J. W. Gilman, T. Kashiwagi, J. E. T. Brown, S. Lomakin, E. P. Giannelis, and E. Manias, *Proceedings of the 43rd International SAMPE Symposium Part I*, **43**, 1053 (1998).
8. V. Kumar and N. P. Suh, *Polym. Eng. Sci.*, **30**, 1323 (1990).
9. W. J. Cho, H. Park, and J. R. Youn, *Journal of Engineering Manufacture, Proc. Instn. Mech. Engrs. Part B*, **208**, 121 (1994).
10. C. Kim and J. R. Youn, *Polymer-Plastics Technology and Engineering*, **39**, 163 (2000).
11. M. S. Koo, K. Chung, and J. R. Youn, *Polym. Eng. Sci.*, **41**, 1177 (2001).

12. W. H. Lee, S. W. Lee, T. J. Kang, K. Chung, and J. R. Youn, *Fiber Polym.*, **3**, 159 (2002)
13. H. Park and J. R. Youn, *Journal of Engineering for Industry, ASME Transactions*, **114**, 323 (1992).
14. H. Park and J. R. Youn, *Polym. Eng. Sci.*, **35**, 1899 (1995).
15. D. Seo, J. R. Youn, and C. L. Tucker III, *International Journal for Numerical Methods in Fluids*, **42**, 1105 (2003).
16. J. R. Youn and H. Park, *Polym. Eng. Sci.*, **39**, 457 (1999).
17. S. Doroudiani, C. B. Park, and M. T. Kortschot, *Polym. Eng. Sci.*, **38**, 1205 (1998).
18. D. F. Baldwin and N. P. Suh, *SPE ANTEC Tech. Papers*, **38**, 1503 (1992).
19. K. A. Seeler and V. Kumar, *J. Reinf. Plast. Compos.*, **12**, 359 (1993).
20. M. Shimbo, D. F. Baldwin, and N. P. Suh, *Polym. Eng. Sci.*, **35**, 1387 (1995).
21. L. M. Matuana, C. B. Park, and J. J. Balatinecz, *Polym. Eng. Sci.*, **38**, 1862 (1998).
22. J. E. Martini, F. A. Waldman, and N. P. Suh, *SPE ANTEC Tec. Papers*, **28**, 674 (1982).
23. S. K. Goel and E. J. Beckman, *Polym. Eng. Sci.*, **34**, 1137 (1994).
24. S. K. Goel and E. J. Beckman, *Polym. Eng. Sci.*, **34**, 1148 (1994).
25. H. J. Lee, M. S. Thesis, Seoul National University, Seoul, 2000.
26. J. Ren, A. S. Silva, and R. Krishnamoorti, *Macromolecules*, **33**, 3739 (2000).
27. J. S. Colton and N. P. Suh, *Polym. Eng. Sci.*, **27**, 485 (1987).
28. Y. Sato, T. Takikawa, S. Takishima, and H. Masuoka, *Journal of Supercritical Fluids*, **19**, 187 (2001).
29. W.-C. V. Wang, E. J. Kramer, and W. H. Sachse, *J. Polym. Sci., Part B., Polymer Physics*, **20**, 1371 (1982).